J. Fluid Mech. (1970), *vol.* 44, *part* 4, *pp.* 637–660
Printed in Great Britain

Turbulent boundary-layer wall-pressure fluctuations on smooth and rough walls

By WILLIAM K. BLAKE
Naval Ship Research and Development Center, Washington, D.C. 20007

(Received 10 November 1969 and in revised form 25 May 1970)

Turbulent boundary-layer wall-pressure measurements were made with 'pinhole' microphones three times smaller (relative to a boundary-layer displacement thickness) than microphones used in earlier work. The improved high-frequency resolution permitted examination of the influence of high-frequency eddies on smooth-wall pressure statistics. It was found that the space-time decay rate is considerably higher than previously reported. Measurements of cross-spectral density made with 5 Hz bandwidth filters disclosed low phase speeds at low frequency and small separation. Measurements were repeated on rough walls and parallels were drawn from knowledge of a smooth-wall boundary-layer structure to propose a structure for a rough-wall boundary layer. The effect of independently varying roughness height and separation on the large and small-scale turbulence structure was deduced from the measurements. It was found that roughness separation affected the very large-scale structure, whereas the roughness height influenced the medium and very small-scale turbulence.

1. Introduction

The studies of pressure fluctuations on walls beneath turbulent boundary layers have been primarily concentrated on smooth-wall flows. The studies are partially directed towards an understanding of the driving force for flow-induced panel flutter and structural vibrations.

The early experiments on smooth-wall boundary layers made by Harrison (1958) were quickly followed by the more elaborate studies of Willmarth & Woolridge (1962) and of Bull (1967) among others. Recently Schloemer (1966) and Bradshaw (1967) studied flows with pressure gradients and Skudrzyk & Haddle (1960) took some pressure spectra on rough surfaces.

All of the above studies were limited by the finite size of the microphone and by extraneous tunnel disturbances. The current re-examination of the smooth-wall pressure statistics was prompted by the availability of a low-noise wind tunnel facility and the capability of achieving better microphone resolution than obtained previously.

The obvious fact that most surfaces are not hydrodynamically smooth prompted the study of rough walls. The experiments were limited to fully rough flow over sand-roughened surfaces; the problem was thus confined to studying the effect of roughness without the difficult complication of considering the viscous effects of smooth-wall to rough-wall transition flows.

2. Experiment description

(a) *Facility description*

All experiments were performed in the subsonic low-turbulence acoustic wind tunnel in the Acoustics and Vibration Laboratory at Massachusetts Institute of Technology. The complete description of this facility is given by Hanson (1969). The inlet contraction led to a 6 ft. long, square duct, 15 in. on a side followed by a 3 ft. long, test section with an identical cross-section as the entrance duct. Measurements were performed on the bottom wall of the test section and sensors were traversed either from the top or bottom of the test section. The smooth test panel was formica-coated plywood and the rough panels were constructed by mounting sand grains to unfinished plywood using shellac as adhesive. For smooth and rough walls, fillets were used to minimize any possible corner flows.

For all experiments, sensors were placed as near as possible to the centre of the test section to avoid sidewall effects; sensors were about 8 in. from sidewalls that contained 2 in. boundary layers.

(b) *Instrumentation*

Velocity measurements. A 0·040 in. diameter flattened-tip total head tube was used for all mean velocity measurements. Traversing was accomplished to 0·01 in. precision and the datum from the smooth wall was determined using a feeler gauge to determine probe-wall contact; from the rough walls by using a machinist's rule graduated to 0·02 in.

The mean velocities were determined from readings obtained on a Betz micromanometer with 0·1 mm of water precision. The total pressure less static wall pressure was measured; static pressure taps were $\frac{1}{10}$ in. diameter tubes mounted flush with the top of the test section. Measured for the smooth wall and the roughest wall ($k_s = 0{\cdot}192$ in.), the static pressure below atmospheric decreased linearly 0·002 in. of water and 0·004 in. of water respectively per inch downstream distance. This pressure gradient affected computations of friction velocity from the momentum integral equation by less than 8 %.

Turbulent velocity fluctuations were measured using a Disa Model 55A32 'X' probe and two 55D05 Disa constant temperature anemometers. The fluctuating signals were amplified in two Ithaco Model 255-A amplifiers; sum and difference of the two anemometer signals were extracted from a Philbrick Q3A1P multiplier-divider and root-mean-square values were determined on a Bruel and Kjaer (B & K) true r.m.s. meter. The probe was positioned to 0.05 in. using a mechanical traverse and this positioning was checked by comparing the mean velocity measured with the anemometer with that measured with the total head tube.

Wall-pressure measurements. The wall-pressure fluctuations were measured using a B & K Model 4138 $\frac{1}{8}$ in. condenser microphone whose sensing area was reduced by placing a cap perforated with a $\frac{1}{32}$ in. diameter hole in its centre over the diaphragm of the microphone. The pinhole perforating the centre of this cap led to a small cavity above the diaphragm. The frequency response of the pinhole

microphone was measured by comparing the response of the microphone with and without the pinhole cap to identical free-field sound fields. The relative phase shift between the microphones was also measured in this manner. A resonant frequency caused by the cavity was measured at about 17·5 kHz. The pinhole microphone response was flat to ± 1 db from 65 Hz to 10 kHz, and the relative phase shift was zero to 5 kHz, 5 degrees at 8 kHz, and 14 degrees at 10 kHz.

The pressure sensitivity at 250 Hz was determined using a B & K Model 4220 pistonphone, which produces an effective free-field sound level of 124 db. Because of the small size of the microphone, the free-field pressure is identical to the pressure at the face of the microphone (Levine & Schwinger 1948) at this frequency so that the calibration is accurate for wall-pressure measurements. The measured sensitivities to ± 1 db are $-83{\cdot}9$ and $-86{\cdot}1$ db reference 1 V/μb for the upstream and downstream microphones respectively.

When in use the microphones were inserted in an aluminium traverse that was mounted flush with the test surface. The traverse consisted of a disk inserted into a rectangular plate. Microphone positioning holes were drilled along a diameter of this disk and filled with plugs when not in use. The positioning holes in addition to a bakelite-lined leading hole provided separations from $\frac{5}{16}$ to 5 in. When fully assembled the traverse plates, plugs, and microphones formed a surface smooth to the touch. The bakelite insulated the fixed leading microphone from the downstream movable microphone. The microphones could be aligned at angles to the flow by turning the traverse disk. For rough-wall measurements sand was mounted directly on the traverse using shellac as adhesive.

The upstream microphone was driven and amplified by a B & K 2107 frequency analyzer while the downstream microphone was driven by a B & K 2801 power supply and its output amplified in an Ithaco amplifier. The relative phase shift through the electronics was negligible to 10 kHz and 3 degrees at 20 kHz. Spectral analysis was performed on a B & K 2107 frequency analyzer using $\frac{1}{10}$ octave filters; the $\frac{1}{10}$th octave levels were corrected to 1 Hz pressure spectra.

Broadband correlations were made in a Model 100 Princeton Applied Research quasi-digital correlator that generated the correlation function as 100 data points for each total time delay that was selected. These functions were plotted on an x, y plotter. The spatial correlations were determined directly from the 1 μsec value of the space-time correlation generated by the correlator. The smoothness of the space-time correlation functions near $\tau = 0$ made it impossible to distinguish between the correlation level at $\tau = 0$ and $\tau = 1$ μsec.

The root-mean-square pressures were determined from an r.m.s. meter, the $\tau = 0$ point of correlation, a graphical integration of the pressure spectral density, and an addition of $\frac{1}{3}$ octave bands of the pressure spectrum. A value obtained through any one of these sources agreed with all other values to within 5 or 6 %.

The cross-spectral densities were determined by using two matched Spectral Dynamics no. 101 heterodyne filters driven by a sweep oscillator. Filter bandwidths of 5 and 50 Hz were used below and above 250 Hz respectively. The data for the rough wall, $k_s = 0{\cdot}106$ in., were generated in a Spectral Dynamics no. 109 co-quad analyzer which computed and plotted the co- and quadrature components simultaneously.

The data for the smooth wall and for the very rough ($k_s = 0{\cdot}192$ in) wall were generated using hybrid instrumentation. In this technique the filter outputs were set either in phase (co-spectrum) or 90 degrees out of phase (quad-spectrum), multiplied using a Philbrick Q3M1P multiplier, and averaged in a Philbrick averaging circuit. The oscillator that was used to drive the filters also drove the x, y plotter so that the co- (or quad-) spectrum was continuously generated. True averaging times for both of the above techniques were 20 sec and 10 sec for the 5 and 50 Hz filters respectively. The cross-spectral densities were normalized using a pressure spectral density measured in the same manner as the cross-spectrum.

(*c*) *Scope and limitations of the measurements*

Measurements of the mean and turbulent velocity profiles and of wall-pressure statistics were made on a smooth wall and two rough walls in order to determine the effects of varying both roughness height and separation on the turbulent field. One wall had densely packed large elements (D-L), the second, sparsely packed small elements (S-S). A third wall with densely packed small elements (D-S) was used to study the effect of sand grain separation independent of grain size; only the mean velocity profile and wall pressure spectral density were measured on this wall.

The broad- and narrow-band measurements were limited by the opposing factors of background noise and microphone frequency response. The pinhole cavity resonance of the microphone band limited the 164 ft./sec smooth wall pressure signal, thus the lower velocity (73, 94, and 124 ft./sec) data were used for broadband measurements on this wall. The cavity resonance affects the reported spectral data to at most ± 1 db, since all data above 10 kHz were discarded. The low frequencies were dominated by an unidentified tunnel disturbance which was of considerable influence to about 70 Hz, also below 70 Hz the microphone response began to decrease so that all spectral data below 70 Hz were discarded.

In order to take full advantage of available wall-pressure signal, cross-spectrum measurements were made at the high velocities, 124 and 164 ft./sec. Since the wall-pressure spectrum level decreases with frequency, and since the level of pressure signal accepted by the filters was set by the broadband level of the input there was not enough correlated signal above $\omega\delta^*/U_\infty \approx 2{\cdot}5$ to analyze reliably.

The acceleration of the microphone-cathode follower system, and the extraneous background noise contributions were estimated with the microphone in place, with the tunnel on, and with the microphone face isolated from the flow. The levels were never significantly higher than the background, tunnel-off level and always more than 15 db below the wall pressure signal.

The usable range for the wall-pressure signal thus extended over the range

$$0{\cdot}06 < \omega\delta^*/U_\infty < 20 \text{ to } 30.$$

(*d*) *Determination of mean wall shear and roughness height*

For all wall conditions the velocity profile U/U_∞ *vs.* $\log y$ was plotted on semi-log paper and y was measured from the datum described in § 2 (*b*); U is the mean

velocity at y and U_∞ is the free-stream velocity. The virtual datum for rough wall measurements is known only through experiment and it is related to the specification of the functional form of U *vs.* y near the wall.

In the smooth-wall case, for small y, U/U_∞ *vs.* $\log y$ formed a straight line whose slope was easily determined. The logarithmic profile is written

$$U/U_\tau = A \log yU_\tau/\nu + B,$$

where U_τ is the friction velocity and A and B are constants. The slope of U/U_∞ *vs.* $\log y$ was then equal to AU_τ/U_∞; when A is selected as 5·75 in accordance with Coles (1956) the slope determines U_τ/U_∞. The constant B was determined from the U/U_τ *vs.* $\log yU_\tau/\nu$ plot.

In the rough wall case U/U_∞ *vs.* $\log y$ did not always form a straight line so that a virtual zero datum was determined by adding constants ϵ to the measured height y until a linear relation, U/U_∞ *vs.* $\log(y+\epsilon)$ was obtained. The slope of this line was 5·75 U_τ/U_∞, where the constant 5·75 was again selected in accordance with Coles (1956). The form of the velocity profile is defined as

$$U/U_\tau = 5{\cdot}75 \log yU_\tau/\nu + B_r,$$

where $B_r = -5{\cdot}75 \log k_s U_\tau/\nu + C$ is different from the smooth wall intercept. C is specified by Schlichting (1956) from Nikuradse's results as 8·5, and it defines k_s, the equivalent sand roughness height.

For the 124 ft./sec condition on each wall U_τ/U_∞ was determined using the momentum integral equation $(U_\tau/U_\infty)^2 = d\theta/dx$ (θ is the momentum thickness and x is streamwise distance); the pressure gradient effect was neglected and both methods of determining U_τ/U_∞ were found equivalent to 5 %. The graphical technique used here has also been used by Perry & Joubert (1963).

(*e*) *Errors in measurement*

The slope of the logarithmic profile has been determined to approximately ± 5 %. The computation of displacement and momentum thicknesses from velocity profiles are reproducible within ± 1·3 % and ± 0·5 % respectively. The error in defining the boundary-layer thickness is related to the error in mean velocity measurement; this causes ± 3 % error in boundary-layer thickness.

The measurements of turbulent velocities are in error by a probe alignment uncertainty of ± 5 degrees by − 2 % to + 5 %. Error in voltage measurement is ± 5 %. The total error in turbulent velocity measurements is thus − 7 % to + 10 %.

The statistical error in using finite averaging times for narrow band analysis has been determined from the relation $\epsilon = 1/(BT)^{\frac{1}{2}}$ (Bendat & Piersol 1966) for the longitudinal and lateral cross-spectral density functions. This is, for a 90 % confidence limit, about ± 20 % for the 5 Hz filter with a 20 sec averaging time and ± 9 % for the 50 Hz filter with a 10 sec averaging time. A constant uncertainty of ± 3 degrees is present in the phase alignment which can cause less than ± 8 % error in low frequency convection velocities. The statistical errors in the value of the computed convection velocities are not easily estimated since mean lines were faired through the spectral data from which the velocities are calculated.

A constant 7 sec averaging time was used for the tenth octave pressure levels; this accounted for ± 13 % statistical error at 100 Hz and 1·3 % statistical error at 10 kHz.

Normalized broadband correlation coefficients contain less than ± 5 % error for high correlation levels and less than ± 10 % error for lowest correlation levels. Microphone positioning was accurate to ± 0·01 in. which is less than ± 4 % at the smallest separation. The associated error in the convection velocities is no more than the 4·5 % error at the closest separation.

3. Results

This section has been subdivided to consider separately the mean velocity, turbulent velocity, and wall-pressure measurements; the smooth and rough walls are considered together in all discussions.

(*a*) *Mean velocity measurements*

The boundary layers considered in this research are all fully-developed self-preserving flows for which the mean velocity distribution, U, in the fully-developed turbulent region of the boundary layer is expressible in the defect form

$$(U_\infty - U)/U_\tau = f(y/\delta), \tag{1}$$

where the friction velocity scale, $U_\tau = (\tau_w/\rho)^{\frac{1}{2}}$ (τ_w is the mean wall shear and ρ is the fluid density), and the boundary-layer thickness, δ, are functions of streamwise position alone. Measurements taken along smooth and rough walls at streamwise station separations at least 4δ apart showed that the self-preserved nature of the flow was indeed closely established.

The rough-wall boundary layers all appropriately fall into the class of fully-developed rough walls for which the streamwise gradient of friction velocity is zero and the hydrodynamic roughness height is a function of x only. The velocity profile is then independent of viscous effects and the wall shear coefficient, τ_w/q (q is the mean dynamic head, $\frac{1}{2}\rho U_\infty^2$, and τ_w is the mean wall shear), is independent of plate Reynolds number, $U_\infty x/\nu$. The flow in the immediate vicinity of the wall is of the form (Clauser 1956)

$$U/U_\tau = A \ln y/l_0 + B, \tag{2}$$

where, for fully rough walls the length scale, l_0, is a characteristic roughness height, k_s, and B is a constant; both are independent of viscosity; and for smooth walls $l_0 = \nu/U_\tau$ and B is a constant. The constant A has been equated to the reciprocal of the von Kármán universal constant, κ, whose most widely accepted values are set within narrow limits; Clauser (1956) states $\kappa = 0{\cdot}41$ and Coles (1956) states $\kappa = 0{\cdot}40$. The value of the constant B is not nearly as well established as the value of κ, and Hinze (1959) cites instances where estimated values of B can range from 3·68 to 5·37. The present results give $B \simeq 4{\cdot}7$. Figure 1 contains the velocity profile in the form of (2) for the smooth wall

$$U/U_\tau = 5{\cdot}75 \log yU_\tau/\nu + 4{\cdot}7.$$

For the rough wall, Schlichting (1956) gives

$$U/U_\tau = 5{\cdot}75 \log y/k_s + 8{\cdot}5,$$

which, presented as a function of yU_τ/ν becomes

$$U/U_\tau = 5{\cdot}75 \log yU_\tau/\nu - 5{\cdot}75 \log k_s U_\tau/\nu + 8{\cdot}5, \tag{3}$$

so that the length scale, k_s, is determined from the roughness defect expressed as

$$\left(\frac{U}{U_\tau}\right)_r - \left(\frac{U}{U_\tau}\right)_s = \frac{\Delta U}{U_\tau} = -5{\cdot}75 \log \frac{k_s U_\tau}{\nu} + 3{\cdot}4, \tag{4}$$

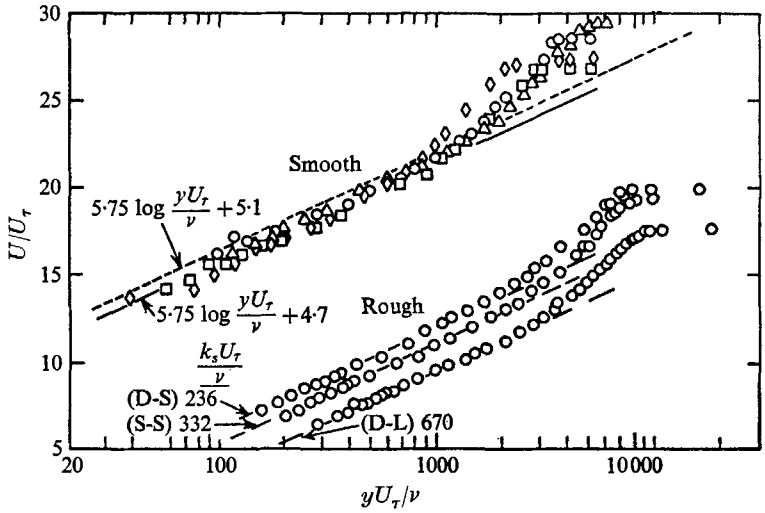

FIGURE 1. Law of the wall for smooth and rough walls. Smooth: ◇, 73 ft./sec; □, 94 ft./sec; ○, 124 ft./sec; △, 164 ft./sec. Rough, all points 124 and 164 ft./sec.

Designation	U_∞ (ft./sec)	k_g (in.)	k_s (in.)	$\delta{\cdot}99$ (in.)	δ^* (in.)	θ (in.)	U_τ/U_∞	R_{e_θ}	$(p^2)^{\frac{1}{2}}/\tau_w$
Smooth	73	—	—	1·8	0·309	0·229	0·0383	$8{\cdot}21 \times 10^3$	3·6
Smooth	94·4	—	—	1·7	0·285	0·228	0·037	$10{\cdot}2 \times 10^3$	3·6
Smooth	124·5	—	—	1·69	0·283	0·226	0·035	$13{\cdot}2 \times 10^3$	3·6
Smooth	164	—	—	1·67	0·280	0·224	0·033	$17{\cdot}0 \times 10^3$	3·6
S-S	124	0·050 0·0625 0·050	0·106	2·36	0·549	0·348	0·0515	$21{\cdot}2 \times 10^3$	3·8
S-S	164	0·0625 0·0845	0·106	2·36	0·576	0·37	0·0515	$29{\cdot}8 \times 10^3$	3·8
D-L	124	0·100 0·0845	0·192	2·42	0·596	0·363	0·0565	$21{\cdot}7 \times 10^3$	3·2
D-L	164	0·100 0·050	0·192	2·42	0·596	0·363	0·0565	$28{\cdot}8 \times 10^3$	3·2
D-S	125	0·0625 0·050	0·0736	2·3	0·522	0·349	0·0502	$21{\cdot}2 \times 10^3$	2·9
D-S	165	0·0625	0·0736	2·3	0·522	0·349	0·0502	28×10^3	2·9

TABLE 1. Mean properties of boundary layers

where the smooth wall intercept, B, has been taken as 5·1 in line with Coles (1956). The rough wall measurements are presented in the form of (3) in figure 1; the values of $k_s U_\tau/\nu$ as determined by (4) are included. The values of all boundary-layer parameters that were measured at the point at which the wall-pressure measurements were taken are shown in table 1.

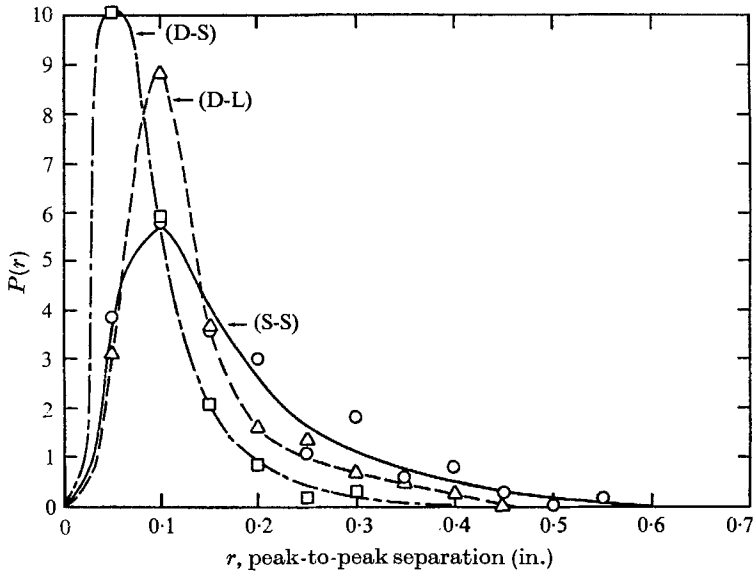

FIGURE 2. Probability density for roughness separations.

Designation	k_g (in.)	$\bar{k}_g$ (in.)	$\bar{r}$ (in.)	$(\bar{r}^2)^{\frac{1}{2}}$ (in.)	σ (in.)	$(\bar{S}^2)^{\frac{1}{2}}/\bar{k}_g$
1. Densely packed large (D-L)	0·0845 0·1	0·092	0·138	0·156	0·0727	0·9
2. Sparsely packed small (S-S)	0·050 0·0625	0·0563	0·172	0·193	0·0876	2·65
3. Densely packed small (D-S)	0·050 0·0625	0·0563	0·085	0·11	0·056	1·34

TABLE 2. Roughness scales

In addition to the specification of an equivalent sand roughness height and an arithmetic mean roughness height for the rough walls, the statistical distribution of protuberance separation was determined. The geometric heights were kept within fairly well-defined limits; the small elements were 16- to 20-mesh grain sizes and the large elements were 10- to 12-mesh grain sizes. These are regarded of uniform heights of 0·0563 in. and 0·0923 in. for the small and large elements, respectively. The separation statistics were determined by measuring the random protuberance separations on the plate to the nearest 0·05 in.; resulting histograms of frequency of occurrence of separations were used to generate the probability densities of figure 2. These probability densities were used to determine the average $\bar{r}$, root-mean-square $(\bar{r}^2)^{\frac{1}{2}}$, and standard deviation σ, of the separations.

The results are shown in table 2. There does not seem to be a definite relation between the statistical length parameters and the equivalent sand roughnesses.

(*b*) *Turbulent velocity measurements*

The root-mean-square levels of the longitudinal (u) and vertical (v) velocity fluctuations were measured for the rough (D-L and S-S) and smooth wall conditions. The turbulent intensities normalized with friction velocity are presented as functions of distance from the wall normalized with boundary-layer thickness in figure 3 (*a*). The smooth-wall data show good agreement with Klebanoff's (1955) profile for which momentum thickness Reynolds number, $U_\infty \theta/\nu$, is comparable to that of the current results.

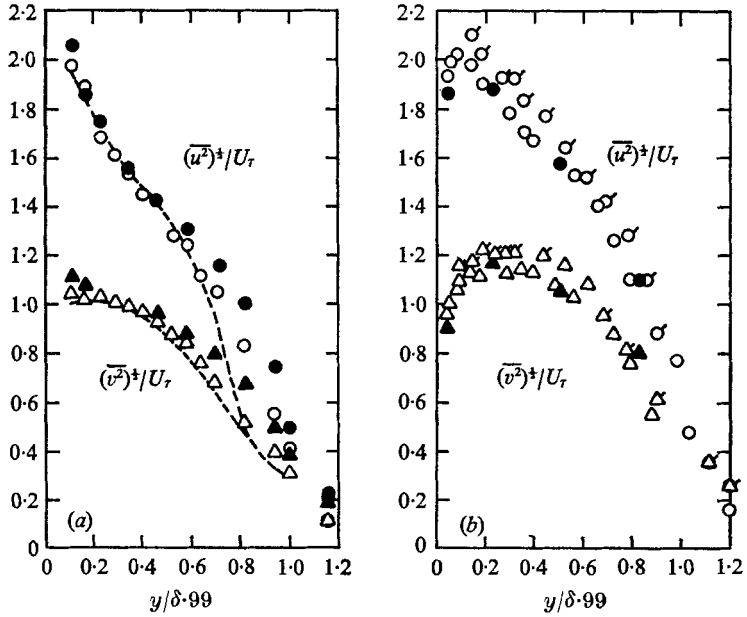

FIGURE 3. Turbulent velocity intensities over smooth and rough, (S-S) and (D-L), walls. O, longitudinal component; △, vertical component; open points 124 ft./sec, closed points 164 ft./sec; flagged points denote (S-S) wall. Dotted line, Klebanoff (1955). (*a*) Smooth. (*b*) Rough.

The intensity profiles for the rough walls are shown in figure 3 (*b*); the rough-wall intensities are slightly higher than the smooth wall intensities, especially in the region about $y = 0{\cdot}1\delta$. Comparison of the data for the (S-S) and (D-L) walls shows that the intensity is higher over the less rough wall. Note, however, that the r.m.s. velocities are increased roughly in proportion to the increase in U_τ.

(*c*) *Turbulent wall-pressure fluctuations*

(i) *Statistical quantities measured.* All wall-pressure measurements are related mathematically to the two-point space-time correlation of wall pressures at a point $\mathbf{x}$ and time t, and at a point $\mathbf{x}+\mathbf{r}$ and time $t+\tau$,

$$R_{pp}(\mathbf{r},\tau) \equiv \langle p(\mathbf{x},t)\, p(\mathbf{x}+\mathbf{r},t+\tau)\rangle, \tag{5}$$

where the brackets in general denote an ensemble average and the correlation is dependent on $\mathbf{x}$ and t co-ordinates. If $R_{pp}(\mathbf{r}, \tau)$ is independent of the $\mathbf{x}$ and t co-ordinates, i.e. when the pressure field is spatially and temporally stationary, the brackets denote a time average. This condition is met in the slowly growing boundary layer when growth is negligible over the distance $\mathbf{r}$.

Information about the spatial translation of frequency components of the wall-pressure field is determined from the cross-spectral density which is the temporal Fourier transform of (5), i.e.

$$\phi(r_i, \omega) = \frac{1}{2\pi} \int_{\infty}^{\infty} R_{pp}(r_i, \tau)\, e^{i\omega\tau}\, d\tau \tag{6}$$

and

$$\phi(r_i, \omega) = |\phi(r_i, \omega)|\, e^{i\alpha(r_i, \omega)}.$$

$\phi(0, 0, \omega)$ is the (real, even) pressure spectral density which is denoted by $\Phi(\omega)$; $\phi(r_1, 0, \omega)$ and $\phi(0, r_3, \omega)$ are real or complex depending on the existence of convection in the r_1 or r_3 directions. Convection was observed in the longitudinal or r_1 direction only. The mean square of the wall pressure, $\overline{p^2}$, is determined by integration of the pressure spectrum, i.e.

$$\overline{p^2} = 2 \int_{0}^{\infty} \Phi(\omega)\, d\omega. \tag{7}$$

The effect of the filter band width on the spectral density measurements has been considered by White (1969) who regards the cross-spectrum as generated by a correlation, $R_{\omega_0}(r_1, \tau)$, of two filtered signals. Thus,

$$R_{\omega_0}(r_1, \tau) = \int_{-\infty}^{\infty} \phi(r_i, \omega)\, |H(\omega)|^2\, e^{-i\omega\tau}\, d\omega, \tag{8}$$

where the filter-shape transfer function,

$$|H(\omega)|^2 = 1, \quad \omega_0 - \tfrac{1}{2}\Delta\omega < |\omega| < \omega_0 + \tfrac{1}{2}\Delta\omega$$

and

$$|H(\omega)|^2 = 0, \quad \text{otherwise.}$$

The filter shape has been idealized to be rectangular, and the form of (8) states that there is no phase shift between the two filters other than that caused by the specified time delay τ. The oddness of the cross-spectrum phase, $\alpha(r_1, \omega)$, in r_1, suggests strongly that $\alpha(r_1, \omega)$ is of the form $k(r_1, \omega)\, r_1$ where k is some equivalent wave-number corresponding to a frequency ω so that we are free to define equivalent phase and group velocities:

$$U_{cp} = \omega/k \quad \text{and} \quad U_{cg} = d\omega/dk. \tag{9}$$

With this distinction, White (1969) shows that when $\Delta\omega/\omega_0$ is not too large the longitudinal cross-spectrum is determined by

$$R_{\omega_0}(r_1, \tau) \simeq 2|\phi(r_1, \omega_0)| \cos[\omega_0(r_1/U_{cp_0} - \tau)] \frac{\sin[\Delta\omega/2\omega_0(r_1/U_{cg} - \tau)\,\omega_0]}{\Delta\omega/2\omega_0(r_1/U_{cg} - \tau)\,\omega_0} \Delta\omega. \tag{10}$$

For the special case of $\Delta\omega/\omega_0 \ll 1$ the $(\sin x/x)$ term approaches unity. By expanding the cosine term, the normalized narrow band correlation coefficient becomes,

$$\frac{R_{\omega_0}(r_1,\tau)}{R_{\omega_0}(0,0)} = \frac{\phi_r(r_1,\omega_0)}{\Phi(\omega_0)}\cos\omega_0\tau + \frac{\phi_i(r_1,\omega_0)}{\Phi(\omega_0)}\sin\omega_0\tau, \tag{11}$$

where $\phi_r = |\phi|\cos(\omega r_1/U_{cp})$ and $\phi_i = |\phi|\sin(\omega r_1/U_{cp})$.

Use of time delays $\tau = 0$ and $\tau = \pi/2\omega_0$ produces either the co- or the quad-spectrum component, and $\alpha(r_1,\omega)$ is then the same as $\omega r_1/U_{cp}$ determined as

$$\omega r_1/U_{cp} = \tan^{-1}\frac{\phi_i(r_1,\omega_0)}{\phi_r(r_1,\omega_0)}. \tag{12}$$

For the current measurements $\Delta\omega/\omega_0$ is of the order of 0·05 or smaller for most frequencies and is of the order of 0·16 near $f = 250$ Hz $(2\pi f = \omega)$, where the change in filter bandwidth from $\Delta f = 5$ Hz to $\Delta f = 50$ Hz was made.

The form of (10) shows that if $R_{\omega_0}(r_1,\tau)$ is measured in broadbands, $\Delta\omega$, and displayed as a function of time delay, τ, for a specified separation, r_1, it would resemble a cosine wave with a phase speed U_{cp} modulated by a wave of effective group speed U_{cg}. The temporal behaviour of $R_{\omega_0}(r_1,\tau)$ shows a maximum that may be more representable as $\tau = r_1/U_{cg}$. In line with this discussion, U_{cg} should be designated a group convection velocity and U_{cp} as a phase convection velocity. White (1969) has shown the pertinence of phase and group velocity distinctions in narrow band measurements.

In the absence of coherence loss, the broadband convection velocity would be defined as the r_1, τ relationship for which

$$\frac{D[R_{pp}(r_1,\tau)]}{D\tau} = \frac{\partial R_{pp}}{\partial\tau} + U_c(r_1,\tau)\frac{\partial R_{pp}}{\partial r_1} = \text{minimum}.$$

The coherence loss of the pressure field makes this relation inapplicable to measurements which provide R_{pp} as a continuous function of τ for discrete values of r_1. In practice an envelope curve is drawn tangent to the peaks of R_{pp} defining a function,

$$r_1 = f(\tau)$$

for the r_1, τ combination for which R_{pp} is a maximum. An 'instantaneous' broadband convection velocity may then be defined as

$$U_c(r_1) = dr_1/d\tau, \tag{13a}$$

and an average broadband convection velocity can then be defined as

$$\bar{U}_c(r_1) = r_1/\tau. \tag{13b}$$

(ii) *Root-mean-square pressure and pressure spectral density.* The wall-pressure spectral density is shown in figure 4 in the dimensionless form

$$\frac{\Phi(\omega)\,U_\infty}{q^2\delta^*} \; vs. \; \frac{\omega\delta^*}{U_\infty},$$

where q is the dynamic head of the free stream. The spectra measured by Willmarth & Wooldridge (1962), Bull (1967), and Schloemer (1966) are all shown

schematically for comparison. The microphone diameter, d, displacement thickness, δ^*, ratio (d/δ^*) is 0·101 to 0·113 for the current smooth-wall measurements; thus the frequency for which $\omega d/2U_{cp}$ is near unity, where a +3 db (Corcos 1963) correction to the measurement is required, is $\omega\delta^*/U_\infty \simeq 10$ and these points are designated in figure 4.

The wall-pressure spectra for all three rough-wall flows are compared with the smooth-wall pressure spectrum in the functional form

$$\frac{\Phi(\omega)\,U_\infty}{\tau_w^2\delta^*} \text{ vs. } \frac{\omega\delta^*}{U_\infty}$$

in figure 5. Spectra for rough- and smooth-wall flows scale well (± 2 db) in the frequency range $0{\cdot}3 < \omega\delta^*/U_\infty < 2{\cdot}5$. The spectra for walls with the smallest roughnesses are practically indistinguishable from the smooth-wall spectrum in this range; the wall with the larger roughnesses (D-L) gives a pressure spectrum slightly lower than the others at low frequencies ($\omega\delta^*/U_\infty < 0{\cdot}3$). At high frequencies there is poor scaling on the variables δ^* and U_∞.

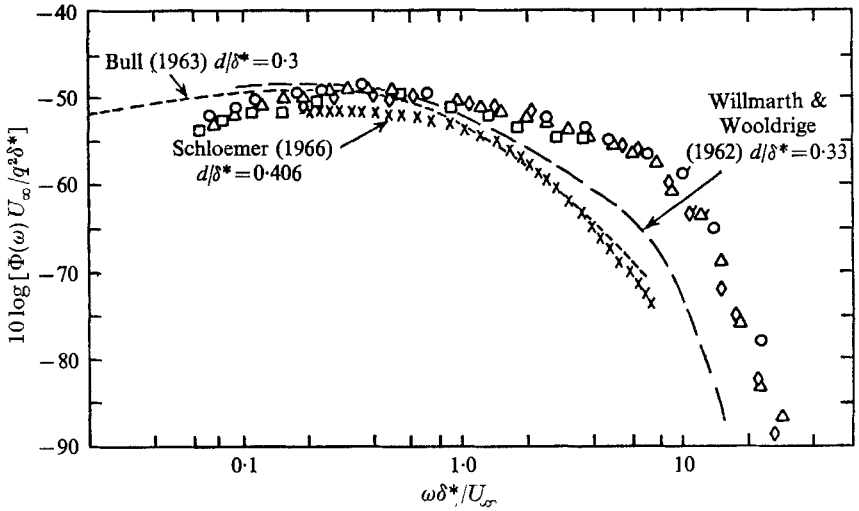

FIGURE 4. Smooth-wall pressure spectrum, outer variables; flagged points denote where $\omega d/2U_c \simeq 1$. Values of U_∞ (ft./sec) and d/δ^*: □, 164, 0·112; ○, 124, 0·110; △, 94, 0·109; ◇, 73, 0·101.

The smooth-wall root-mean-square pressure (7), $(\overline{p^2})^{\frac{1}{2}}$, is $8{\cdot}76 \times 10^{-3}q$ or $3{\cdot}59\tau_w$ which is considerably higher than that reported by other investigators. This higher value is consistent with the improved microphone resolution of the current measurements. The root-mean-square pressures for the rough walls depend on roughness height and table 1 shows the computed values normalized on mean wall shear stress. The pressure spectra all peak at approximately the same level, $\Phi(\omega)\,U_\infty/(\tau_w^2\delta^*) \simeq 0{\cdot}2$, so that differences in r.m.s. pressure are primarily caused by differences in the bandwidths of the pressure spectra. The spectra become more peaked for an increase in roughness, see figure 5. An average of the results is $(\overline{p^2})^{\frac{1}{2}}/q \simeq 3{\cdot}4C_f$ for smooth and rough walls where $C_f = \tau_w/q$.

It is assumed that the rough-wall pressure spectrum is negligibly affected by microphone size effects. The value of d/δ^* for the rough-wall measurements is about 0·05 and the frequency at which the microphone diameter equals a half wavelength (requiring roughly a +3 db Corcos correction to the spectrum) corresponds to $\omega\delta^*/U_\infty \simeq 30$; above this frequency the rough-wall pressure spectrum was not measured.

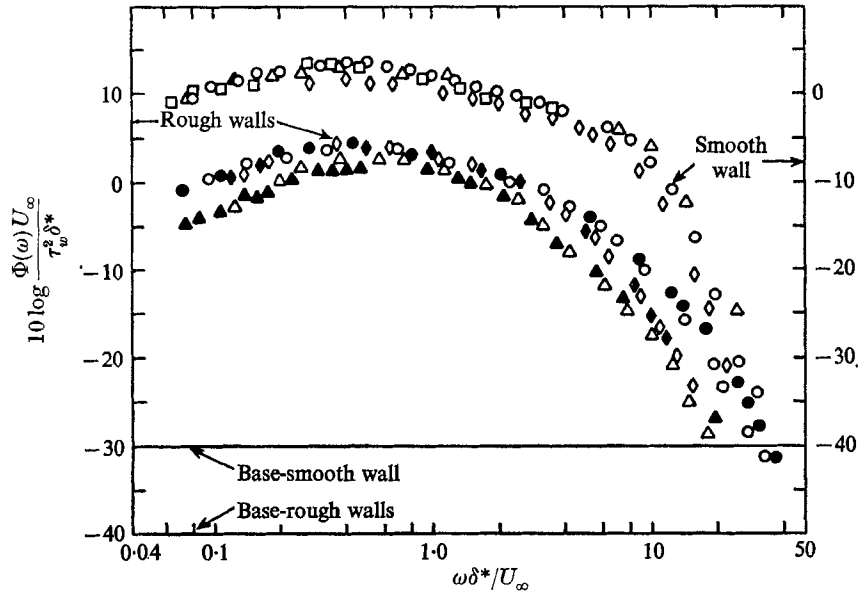

FIGURE 5. Wall-pressure spectra over smooth and rough walls, outer variable scaling (note the shift in base lines). Smooth wall, U_∞ (ft./sec): ◇, 73; ○, 94; △, 124; □, 164. Rough wall: open points 124 ft./sec; closed points 164 ft./sec; ◇, ◆, (D-S); ●, ○, (S-S); ▲, △, (D-L).

(iii) *Broadband spatial correlations.* The smooth-wall longitudinal spatial correlation is shown in figure 6, and shows a more rapid coherence loss than do the results reported by Bull and Willmarth & Wooldridge. The inclusion o uncorrelated high-frequency wall pressure components into the measurement causes more rapid normalized correlation decay. For the rough walls the longitudinal spatial correlations are similar to those obtained with the smooth wall, but show a slightly more rapid loss of positive coherence.

The lateral spatial correlations are also shown with the smooth wall values in figure 6. In contrast to the longitudinal correlations, the lateral correlations show negligible wall effect probably because the laterally correlated pressure eddies are generated some distance upstream of the microphone system. For the microphone separations used ($r_3 > 0{\cdot}8\delta^*$), these correlations are then determined by the low frequency outer flow eddies whose characteristics are set by boundary-layer size, not by local wall condition.

(iv) *Broadband space-time correlations and convection velocities.* Representative space-time correlations are shown in figure 7 for the smooth wall ($U_\infty = 73$ and 124 ft./sec) and in figure 8 for the rough walls ($U_\infty = 124$ and 164 ft./sec). The correlation shapes show clearly the non-frozen convection pattern of the pressure

field. The peaks broaden and become progressively unsymmetrical due to the decay of the lower velocity, smaller eddies and the resulting predominance of the larger, higher speed eddies. The space-time decay rates are similar for both wall flows, the smooth wall decay envelope, or 'moving axis correlation' for the smooth wall is shown in each figure.

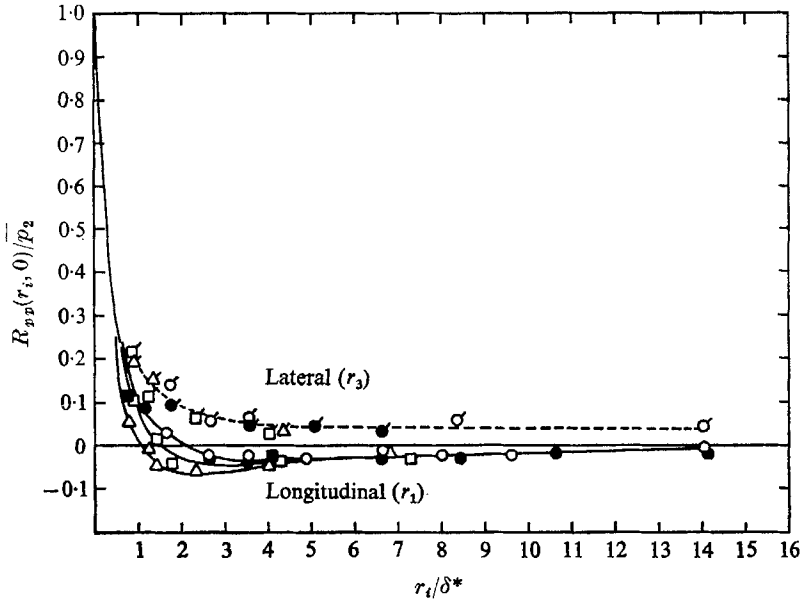

FIGURE 6. Longitudinal and lateral broadband spatial correlations, smooth and rough walls. Smooth walls U_∞ (ft./sec): ○, 94; ●, 124. Rough wall: open points 124 ft./sec; closed points 164 ft./sec; △, ▲, (S-S); □, ■, (D-L).

The average ($\overline{U}_c$) and the instantaneous (U_c) convection velocities, determined using (13*a*) and (13*b*), increase with streamwise separation in excellent agreement with Bull's (1967) and Willmarth & Wooldridge's (1962) results (see figure 9(*a*)). The 'instantaneous' smooth wall convection velocity very slowly approaches $0{\cdot}82U_\infty$; this reflects the decay of slower small-scale pressure sources and gradual domination by higher speed sources at large separations. The convection velocities for the rough walls (figure 9(*b*)) are somewhat lower and approach an asymptotic value ($0.73U_\infty$) in a shorter distance ($r_1/\delta^* \simeq 4$) than over smooth walls. The lower speed pressure sources apparently lose coherence in a shorter distance over rough than over smooth walls. The reduction in convection velocities, both mean ($\overline{U}_c$) and instantaneous (U_c), caused by roughness is expressible in terms of a velocity defect,

$$(U_c/U_\tau)_s - (U_c/U_\tau)_r = \Delta U_c/U_\tau = \Delta\overline{U}_c/U_\tau.$$

For either the $r_1 \to \infty$ or the $r_1 \to 0$ limits the values of the defect are 9·2 for the (S-S) wall and 10·5 for the (D-L) wall; the mean velocity defects $\Delta U/U_\tau$ (equation (5)) for the rough walls are 10 for the (S-S) wall and 11·5 for the (D-L) wall.

(v) *Cross-spectral density and narrow band convection velocity measurements.* The normalized magnitude of the longitudinal cross-spectral density functions are shown for all walls in figure 10; they were determined by using (11) for very narrow bandwidths. For all walls, the longitudinal amplitude functions collapse well on the phase angle $\alpha(r_1, \omega)$, as determined by (12) and would collapse as

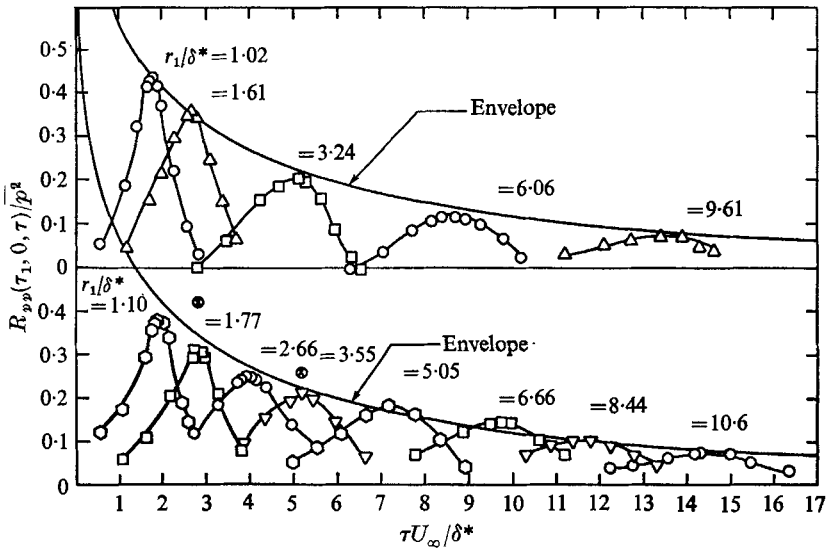

FIGURE 7. Smooth-wall pressure broadband longitudinal space-time correlations. Lines are moving axis correlations; points designated by ⊗ were computed from the cross-spectral density. Top diagram U_∞ = 73 ft./sec; bottom diagram U_∞ = 124 ft./sec.

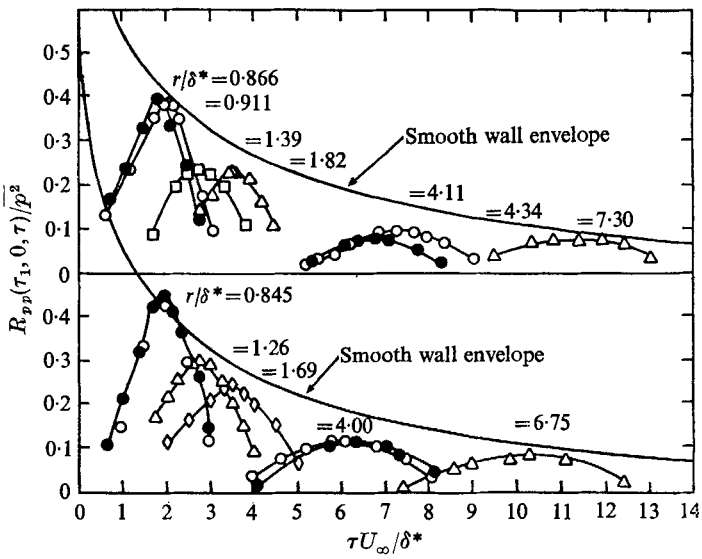

FIGURE 8. Rough-wall pressure broadband longitudinal space-time correlations. Lines are the smooth wall envelopes, moving axis correlations, from figure 7. Open points 124 ft./sec; closed points 164 ft./sec. Top diagram (S-S) wall; bottom diagram (D-L) wall.

well on $r_i\omega/U_\infty$ ($i = 1$ or 3). The former representation may be given physical interpretation when the phase angle, $\alpha(r_1, \omega)$, is given the form $kr_1 = \omega r_1/U_{cp}$. The amplitude function then describes the persistence of a dominant wave-number, $\omega/U_{cp}(r_1, \omega)$, or of a pressure producing eddy observed in a frame of reference moving with the eddy. Presentation of the data as a function of $\omega r_1/U_\infty$, however,

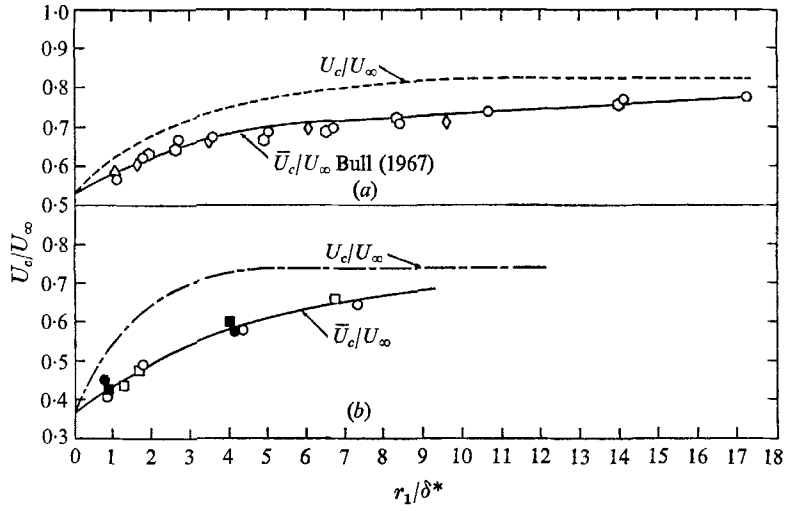

FIGURE 9. Broadband wall pressure convection velocities. (*a*) Smooth: ◊, 73 ft./sec; ○, 94 ft./sec; ○, 124 ft./sec. (*b*) Rough: ○, (S-S) wall; □, (D-L) wall; open points, 124 ft./sec; closed points, 164 ft./sec.

provides a measure of the pressure field coherence loss independent of an assumed wave-like nature. The lateral cross-spectral density amplitude functions were obtained using (11) and they are shown as functions of $\omega r_3/U_{cp}$ in figure 11. Since there was no detectable lateral convection U_{cp} was obtained from the longitudinal measurements. The $\omega r_1/U_{cp}$ interpretation of figures 10 and 11 shows a coherence loss (determined at a cross-spectrum level of 0·10) longitudinally in about three wavelengths over smooth walls, 1·2 wavelengths over the (S-S) wall, and one wavelength over the (D-L) wall; lateral coherence is lost in about $\frac{1}{2}$ wavelength over all walls.

The narrow band convection velocities for all walls determined as

$$U_{cp} = r_1\omega/\alpha(r_1, \omega)$$

are shown in figures 12. Very low-phase speeds at low frequencies are observed over all walls and the phase speeds increase with frequency and microphone separation, reach a maximum, and then asymptote to some intermediate value. The smooth-wall convection velocities can be as high as $0{\cdot}8U_\infty$ and asymptote to $0{\cdot}53U_\infty$ as determined by Bull (1967). The rough-wall convection velocities are lower than those over the smooth walls at any frequency and they are lowest over the rougher of the two walls. The high-frequency asymptotes are about $0{\cdot}46U_\infty$ for the (S-S) wall and $0{\cdot}44U_\infty$ for the (D-L) wall. As for all the broadband convection velocity asymptotes, the differences in convection velocity over rough

walls from those measured over smooth walls are determined by the velocity defect caused by the wall roughness.

The smooth wall cross-spectra are in close agreement with those obtained from the data of Willmarth & Wooldridge by Corcos (1963). Agreement with Bull's (1967) $\frac{1}{3}$-octave band results is good in general, but the current results do not

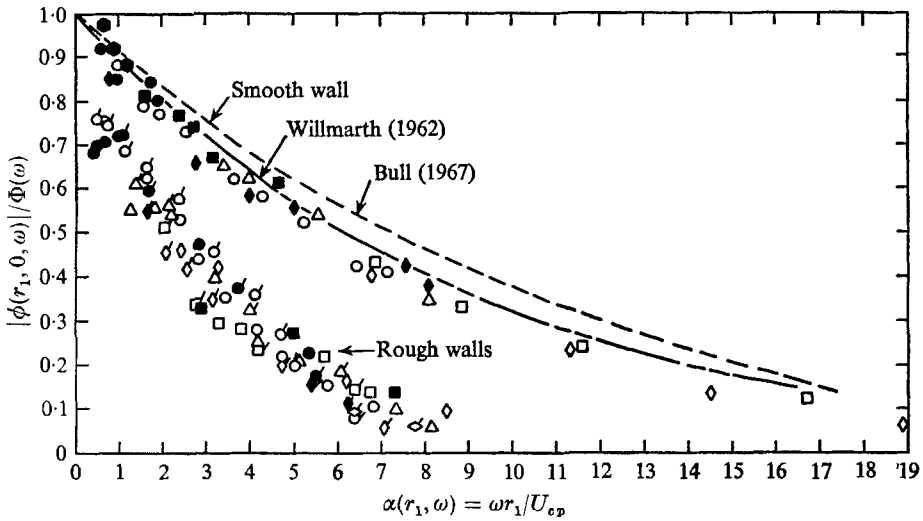

FIGURE 10. Normalized longitudinal cross-spectral density for smooth and rough walls. Smooth-wall points for r_1/δ^*: ○, 1·77; ◇, 2·67; △, 3·55; □, 8·41; ◇, 14·2. (S-S) rough-wall points for r_1/δ^*: ○, 0·914; △, 1·828; ◊, 4·33; □, 7·4. (D-L) rough-wall points for r_1/δ^*: ○, 0·845; △, 1·23; □, 1·69; ◊, 4·0; ◇, 6·75. Open points; 124 ft./sec; closed points 164 ft./sec.

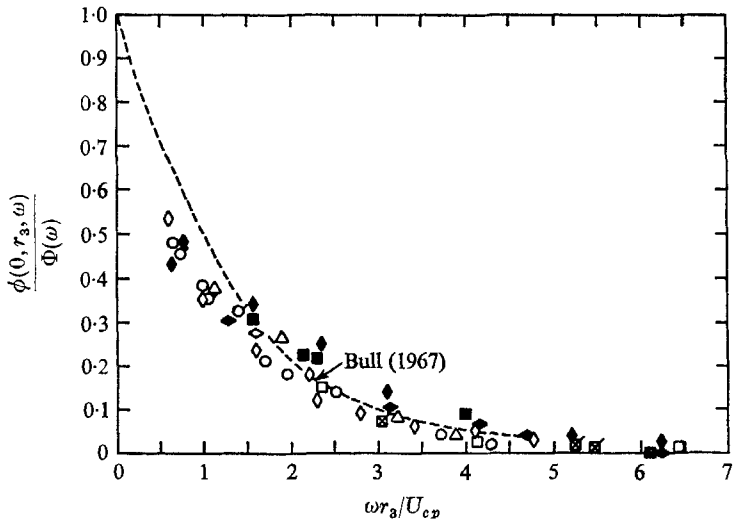

FIGURE 11. Normalized lateral cross-spectral density amplitude for smooth and rough walls. Smooth-wall points for r_3/δ^*: ○, 1·77; △, 3·55; ⊠, 8·41. (S-S) rough-wall points for r_3/δ^*: ◊, 0·196; □, 4·03. (D-L) rough wall points for r_3/δ^*: ◊, 0·845; □, 1·23; ◇, 1·69. Open points, 124 ft./sec; closed points, 164 ft./sec.

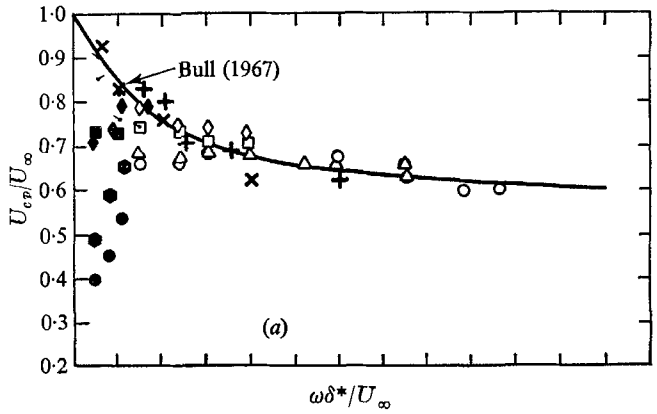

FIGURE 12(*a*). Phase and group convection velocities. Smooth wall. Group velocities: 126 ft./sec, values of r_1/δ^*: +, 1·77; ⬮, 8·41; ⬮, 14·2; 164 ft./sec: ×, 2·67. Phase velocities: open points 126 ft./sec; closed points 164 ft./sec. Values of r/δ^*: ○, 1·77; ●, 1·78; ▲, 2·67; △, 3·55; □, ■, 8·41; ◇, ◆, 14·2.

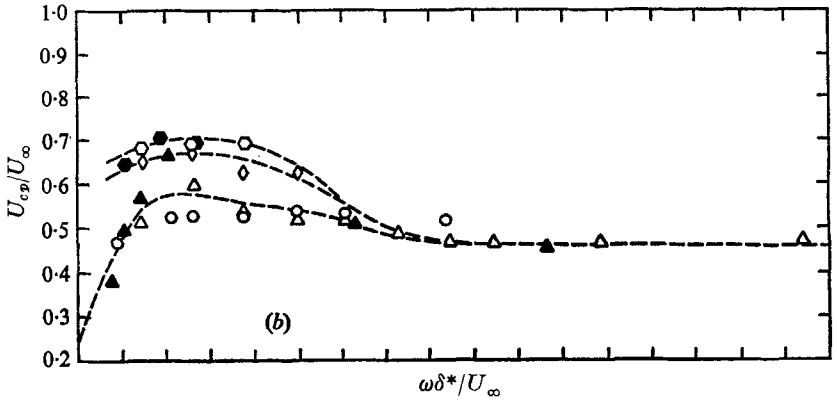

FIGURE 12(*b*). Phase convection velocities. Rough wall (S-S). Open points 124 ft./sec closed points 164 ft./sec. Values of r_1/δ^*: ▲, △, 0·914; ○, 1·828; ◇, 4·33; ⬮, ⬭, 7·4.

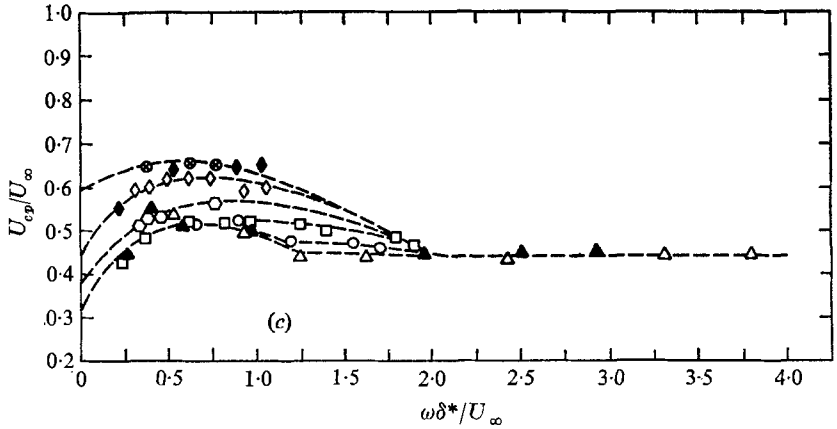

FIGURE 12(*c*). Phase convection velocities. Rough wall (D-L). Open points 124 ft./sec; closed points 164 ft./sec. Values of r/δ^*: ▲, △, 0·845; ○, 1·23; □, 1·69; ⬭, 2·32; ◆, ◇, 4·0; ⊗, 6·75.

show the lack of $\omega r_1/U_{cp}$ and $\omega r_3/U_{cp}$ similarity at low frequencies as reported by Bull. The smooth-wall phase velocities shown in figure 12 (*a*) agree with Bull's (1967) data for frequencies above $\omega\delta^*/U_\infty = 0{\cdot}3$. The solid line attributed to Bull in figure 12 (*a*) is that which he drew through his data. The current measurements show clearly that the convection velocities measured with small separations decrease sharply with decreasing frequency and show considerably less frequency dependence when measured with large separations. Throughout the region of low frequency dependence, the convection velocities increase with increasing separation. This disagreement with Bull's low frequency results is probably due to differences in bandwidth effect; when a 50 Hz filter rather than a 5 Hz filter was used for low frequency measurements, low frequency cross-spectrum and convection velocity behaviour similar to that found by Bull was obtained.

In line with this bandwidth discussion and that of § 3 (*c*) (i), if Bull's results are interpreted as group convection velocities and the current measurements as phase convection velocities, we can relate group and phase velocities using their definitions, (9), so that

$$\frac{d}{d\omega}\left(\frac{1}{U_{cp}}\right) = \frac{1}{\omega}\left(\frac{1}{U_{cg}} - \frac{1}{U_{cp}}\right) = \frac{1}{U_{cp}^2}\frac{dU_{cp}}{d\omega},$$

which gives the non-dimensional form

$$\frac{U_{cg}}{U_\infty} = \left(\frac{U_{cp}}{U_\infty}\right)^2 \Big/ \left[\frac{U_{cp}}{U_\infty} - \frac{\omega\delta^*}{U_\infty}\frac{d(U_{cp}/U_\infty)}{d(\omega\delta^*/U_\infty)}\right]. \tag{14}$$

Group velocities determined from faired curves drawn through points in figure 12 (*a*) using (14) are summarized in figure 12 (*a*) by the designated symbols which approach $0{\cdot}9U_\infty$ at low frequencies and which are practically indistinguishable from phase velocities at frequencies above $\omega\delta^*U_\infty = 1$ since $dU_{cp}/d\omega \simeq 0$ there. Large bandwidth (50 c/sec) measurements made in the early stages of this work further substantiate this interpretation; convection velocities on the order of $0{\cdot}9U_\infty$ were measured at low frequencies.

4. Discussion of characteristics of the smooth- and rough-wall pressure fields

The wall-pressure field may be considered as generated by sources that are distributed throughout the boundary layer and whose dynamics are determined by length and velocity scales characteristic of the region of the boundary layer in which the sources exist. An effective source location is determined as that position in the boundary layer for which the convection velocity at a frequency is identical to the mean velocity, i.e. $U_{cp}(\omega) = U(y)$ and y is the location of the source moving at speed $U_{cp}(\omega)$ which causes a pressure spectrum level at frequency ω.

Inner and outer length and velocity scales are used to describe the dynamics of pressure sources located near to and far from the wall. Thus for the smooth-wall pressure spectrum, outer and inner variables respectively can be used to represent viscous (ν, U_τ) and inviscid (δ^*, U_∞) influences of inner and outer boundary-layer

dynamics. Comparison of figures 4 and 13 shows that outer variables rather than inner variables determine the pressure levels at low frequencies. Rough-wall pressure spectra, represented in terms of outer and inner variables in figures 5

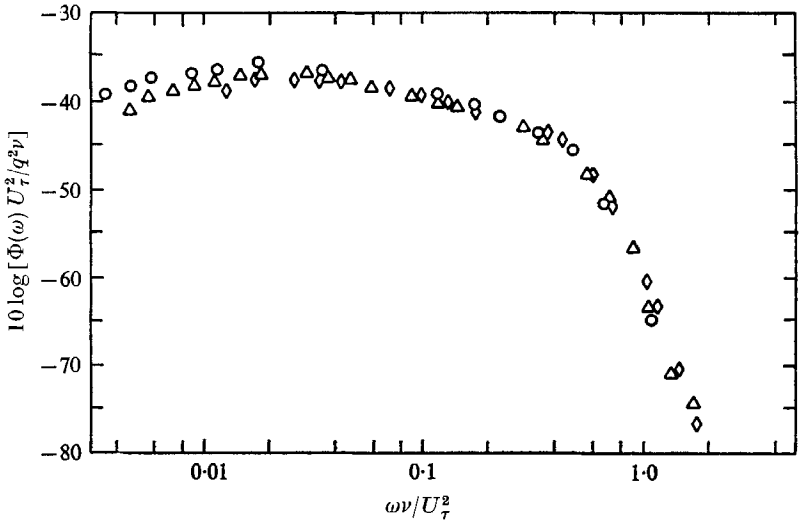

FIGURE 13. Smooth wall pressure spectrum, inner variables. Values of U_∞ and R_{e_θ}: ◇, 73, 8200; △, 94, 10,200; ○, 124, 13,200.

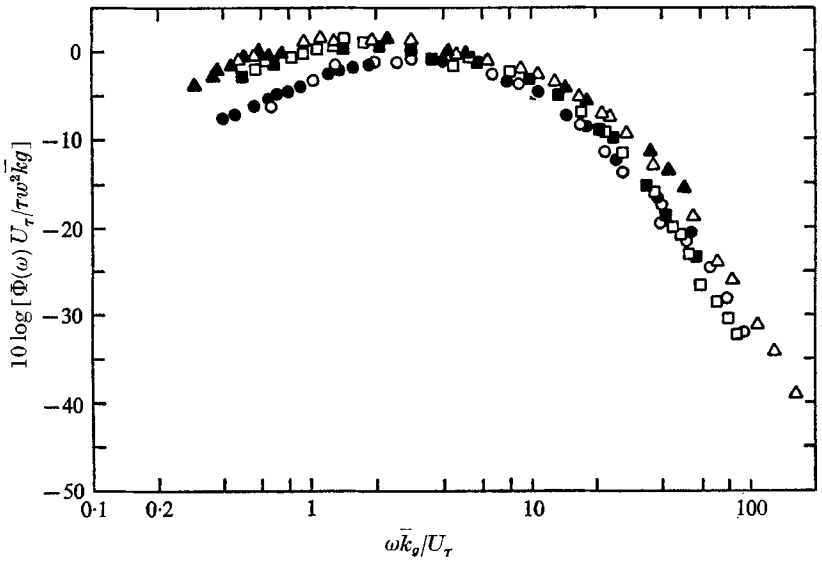

FIGURE 14. Rough wall pressure spectrum, inner variables. ○, (D-L) wall; △, (S-S) wall; □, (D-S) wall; open points, 124 ft./sec; closed points, 164 ft./sec.

and 14, are best described by δ^* and $\bar{k}_g$, the arithmetric mean roughness height. Values of $\bar{k}_g$ for each wall are given in table 2. Note that the pressure spectrum in figure 9 has been normalized with mean wall shear τ_w and this normalization brings the maximum spectrum levels of smooth and rough walls into coincidence.

In the absence of pressure gradients, wall shear is the only external stress on the boundary layers, and this stress apparently determines the level of fluctuating pressure exerted on a wall by eddy motion in the boundary layer. Comparison of figures 5 and 14 shows that the high frequency rough wall pressure spectra are best expressed in terms of roughness height, but that the moderate and low frequency spectra are best described by δ^*. At very low frequencies, however, δ^* does not bring the (D-L) wall pressure levels into coincidence with those over the (D-S) and (S-S) walls. Furthermore, figure 14 shows that $\bar{k}_g$ scaling shows a gradual increase in spectrum level that may be determined by roughness spacing relative to roughness size.

A semi-quantitative measure of roughness element spacing can be simply defined by assuming uniform roughness size, statistical independence of spacing and size, and by considering the roughness elements as cubical particles. The statistical interstice dimension is defined as the mean-square void size written

$$\overline{S^2} = \overline{(r-\bar{k}_g)^2} = \overline{r^2} + \bar{k}_g^2 - 2\overline{rk_g},$$

where r is the roughness separation and $\overline{k_g}$ is the mean roughness height and breadth. The ratio of root-mean-square void size, $(\overline{S^2})^{\frac{1}{2}}$, to average geometric height is a comparative qualitative indication of turbulent flow rate possible between roughness elements. Thus, using the roughness statistics from table 2, the quantity

$$(\overline{S^2})^{\frac{1}{2}}/\overline{k_g} = (\overline{r^2}/\bar{k}_g^2 + 1 - 2\bar{r}/\overline{k_g})^{\frac{1}{2}}$$

may be computed. The relative interstice size is 0·9 for the (D-L) wall, 2·65 for the (S-S) wall and 1·34 for the (D-S) wall. The roughness size determines the average eddy size, and the interstice size determines the range of eddy sizes that exist between protuberances. A large relative interstice size, then, indicates that a large range of eddy sizes can exist between protuberances; the limit of vanishing interstice size is the smooth wall. The breadth of the wall-pressure spectra for each rough wall increases with relative intersticial size. The means by which interstice size can effect the low-frequency pressure fluctuations is, however, very much open to question.

Since the effectiveness of the scaling parameters in determining pressure spectrum levels and coherence losses depends on the location of pressure producing eddies in the boundary layer, the phase convection velocity (U_{cp}) data in figure 12 (*a*) can be used to give further insight into the pressure source locations and behaviour. At low frequencies the strong dependence of U_{cp} on microphone separation and frequency is accompanied with a spread in the pressure spectrum level that is better described in terms of outer rather than inner variables. The very low phase velocities (figure 12 (*a*)) at low frequencies that are strongly dependent on microphone separation and that vary from $0{\cdot}4U_\infty$ to $0{\cdot}75U_\infty$ do not permit assignment of locations for the dominant pressure sources. At moderate frequencies where U_{cp} is maximum and shows more microphone separation dependence than frequency dependence, the spectrum levels are highest and the pressure sources are located at distances from the wall of $0{\cdot}1\delta$ to $0{\cdot}3\delta$. This is the transition region of the boundary layer between the constant-stress and wake regions where inner (ν/U_τ or $\bar{k}_g$, U_τ) scaling gives way to outer (δ or δ^*, U_∞) scaling.

At higher frequencies the phase convection velocities decrease and apparently asymptote to some value that slowly varies with frequency. These pressure sources are located within the constant stress region (see figures 13 and 14), $y < 0{\cdot}1$, so that inner variables scale the pressure spectra. At very high frequencies, $\omega\bar{k}_g/U_\tau > 20$, the pressure spectrum for the (S-S) wall is higher than the spectra for the (D-L) and (D-S) walls so that roughness separation appears to have some influence on this part of the spectrum. The relative interstice size is somewhat higher for the (S-S) wall than it is for the other walls and this may be reflected in the higher pressure levels at high frequencies for this wall. The longitudinal cross-spectral density results (figure 10) show that the inner layer (high frequency) pressure eddies lose coherence over rough walls much more rapidly than over smooth walls; this is indicated by the more rapid longitudinal cross-spectrum amplitude decay over rough walls (figure 10). Lateral coherence loss, indicated in figure 11, is similar over both wall types.

There is evidence that, at moderately high frequencies where the pressure sources are near $y < 0{\cdot}18$ and where U_{cp} has not yet reached its asymptote, the spectra on all walls behave as $\Phi(\omega) \sim \omega^{-1}$ which requires that (Bradshaw 1967) the pressure spectrum level and wave-number (ω/U_{cp}) are determined solely by the wall shear and source position respectively. In this connexion $\omega y/U_{cp} \simeq$ constant where y is the effective source location defined earlier. Bradshaw's (1967) dimensional analysis for pressure sources in the constant stress region can be put into a non-dimensional form $\Phi(\omega\nu/U_\tau^2)\, U_\tau^2/q^2\nu$ proportional to $(\omega\nu/U_\tau^2)^{-1}$. The spectra of figures 4 and 13 show $\omega^{-0{\cdot}75}$ dependence; Hodgeson, as reported by Bradshaw (1967), found $\omega^{-0{\cdot}72}$ behaviour. The current results show this dependence to extend to $\omega\delta^*/U_\infty = 5$ which is upper limit of $\omega y/U_c =$ constant validity.

The rough-wall pressure spectra, scaled on outer (δ^*, U_∞) variables, depart from the spectrum of the (S-S) condition at $\omega\delta^*/U_\infty \simeq 2{\cdot}8$ and $4{\cdot}3$ for the (D-L) and (D-S) walls respectively (see figure 5). These frequencies correspond to a single 'Strouhal number', $f\bar{k}_g/U$, of about $0{\cdot}17$ where $U \simeq 0{\cdot}45U_\infty$ is the approximate high frequency convection velocity asymptote for the walls. This common 'Strouhal number' suggests a mechanism in rough-wall turbulence production that is analogous to wake formation. Furthermore, these frequencies correspond to values of $\omega\bar{k}_g/U_\tau$ equal to $7{\cdot}7$ and $9{\cdot}2$ which fall well within the inner variable scaling region. It is apparent that the high-frequency rough-wall pressures are strongly dependent on flow conditions very near the roughness elements; they depend on the height and, to a lesser extent, on the separation of elements.

5. Conclusions

The major conclusions reached in this investigation are:

The high-frequency pressure levels are determined by length and velocity scales characteristic of the constant stress region in which the corresponding pressure sources for these levels are located. For the rough walls these scales are determined by experiment to be the average geometric roughness height and the

friction velocity; for the smooth and rough walls they are ν/U_τ and U_τ. The low-frequency pressure levels on smooth and rough walls are adequately scaled on outer flow parameters U_∞ and δ^*; rough- and smooth-wall pressure spectra have a common maximum level when scaled on wall shear.

The sources for very low frequency pressure generation on smooth and rough walls appear to be similar in some respects; however, the natures of the sources are not indicated by these measurements. The sources for pressures at moderate frequencies are in the constant stress region and behave similarly on smooth and rough walls. High-frequency pressure production is possibly determined by a wake-like phenomenon near the roughness tops; roughness height and, to a lesser extent, separation determine the high frequency wall pressure levels.

The lower convection velocities measured over rough walls are a direct result of the retardation of the mean boundary-layer motion caused by the presence of roughness on the wall. The convection velocity defect scaled on friction velocity is to a good approximation the same as the defect of the mean velocity profile caused by roughness.

The coherence loss of inner flow pressure eddies is apparently determined by a viscous length scale on smooth walls, and roughness height on rough walls. In both cases coherence is lost due to high production rates near the wall that are characteristic of the wall type. The outer flow broadband coherence loss is similar for smooth and rough walls but, the inner flow coherence loss over rough walls is considerably higher than over smooth walls.

The wall-pressure levels in smooth and rough walls are established by the wall shear level. The r.m.s. pressure is approximately $(\overline{p^2})^{\frac{1}{2}}/q \simeq 3{\cdot}4C_f$ for both wall types.

The author expresses his indebtedness to Professor P. Leehey, chairman of his doctoral thesis committee, and to Dr R. Lyon and Professor S. Windall, members of the committee at Massachusetts Institute of Technology for their many helpful suggestions made during the course of this work. The research was carried out at the Department of Naval Architecture, Massachusetts Institute of Technology under the Naval Ship Systems Command, General Hydromechanics Research Program, Contract N00014-67-A-0204-0002, administered through the Naval Ship Research and Development Center, Washington, D.C.

REFERENCES

Bendat, J. S. & Piersol, A. G. 1966 *Measurement and Analysis of Random Data*. Wiley.
Bradshaw, P. 1967 *J. Fluid Mech.* **30**, 241.
Bull, M. K. 1967 *J. Fluid Mech.* **28**, 719.
Clauser, F. H. 1956 *Adv. Appl. Mech.* **4**, 1.
Coles, D. 1956 *J. Fluid Mech.* **1**, 191.
Corcos, G. M. 1963 *J. Acoust. Soc. Am.* **35**, 192
Hanson, C. E. 1969 *Acoustics and Vibration Lab MIT Rep.* no. 79611-1.
Harrison, H. 1958 *2nd Symposium of Naval Hydrodynamics*, 107.
Hinze, J. O. 1959 *Turbulence*. McGraw-Hill.
Klebanoff, P. S. 1955 *NACA Rep.* no. 1247.

KLINE, S. J., REYNOLDS, W. C., SCHRAUB, F. A. & RUNSTADLER, P. W. 1967 *J. Fluid Mech.* **30**, 741.

LEVINE, N. & SCHWINGER, J. 1948 *Phys. Rev.* **73**, 383.

PERRY, A. E. & JOUBERT, P. N. 1963 *J. Fluid Mech.* **17**, 193.

SCHLICHTING, H. 1956 *Boundary Layer Theory*. McGraw-Hill.

SCHLIEMER, H. H. 1956 *U.S. Navy Underwater Sound Laboratory Rep.* no. 747.

SKUDRZYK, E. J. & HADDLE, G. P. 1960 *J. Acoust. Soc. Am.* **32**, 19.

WHITE, P. 1969 *J. Acoust. Soc. Am.* **45**, 1118.

WILLMARTH, W. W. & WOOLDRIDGE, C. E. 1962 *J. Fluid Mech.* **14**, 187.